Maleki *et al. Journal of Biological Engineering* (2024) 18:49
https://doi.org/10.1186/s13036-024-00445-0

Journal of Biological Engineering

RESEARCH

Open Access

Investigation of pH-dependent Paclitaxel delivery mechanism employing Chitosan-Eudragit bioresponsive nanocarriers: a molecular dynamics simulation

Reza Maleki[1*], Mohammad Khedri[2], Sima Rezvantalab[3] and Nima Beheshtizadeh[4,5*]

Abstract

Before embarking on any experimental research endeavor, it is advisable to do a mathematical computation and thoroughly examine the methodology. Despite the use of polymeric nanocarriers, the regulation of bioavailability and drug release at the disease site remains insufficient. Several effective methods have been devised to address this issue, including the creation of polymeric nanocarriers that can react to stimuli such as redox potential, temperature, pH, and light. The present study has been utilized all-atom molecular dynamics (AA-MD) and coarse-grained molecular dynamics (CG-MD) methods and illustrated the drug release mechanism, which is influenced by pH, for Chitosan-Eudragit bioresponsive nanocarriers. The aim of current work is to study the molecular mechanism and atomistic interactions of PAX delivery using a Chitosan-Eudragit carrier. The ability of Eudragit polymers to dissolve in various organic solvents employed in the process of solvent evaporation is a crucial benefit in enhancing the solubility of pharmaceuticals. This study investigated the use of Chitosan-Eudragit nanocarriers for delivering an anti-tumor drug, namely Paclitaxel (PAX). Upon analyzing several significant factors affecting the stability of the drug and nanocarrier, it has been shown that the level of stability is more significant in the neutral state than the acidic state. Furthermore, the system exhibits higher stability in the neutral state. The used Chitosan-Eudragit nanocarriers exhibit a stable structure under alkaline conditions, but undergo deformation and release their payloads under acidic conditions. It was demonstrated that the in silico analysis of anti-tumor drugs and carriers' integration could be quantified and validated by experimental results (from previous works) at an acceptable level.

Keywords Drug release mechanism, Chitosan nanoparticles, PH-dependent release, Drug delivery

*Correspondence:
Reza Maleki
rmaleki@irost.ir
Nima Beheshtizadeh
n.beheshtizadeh@tbzmed.ac.ir
Full list of author information is available at the end of the article

Graphical abstract

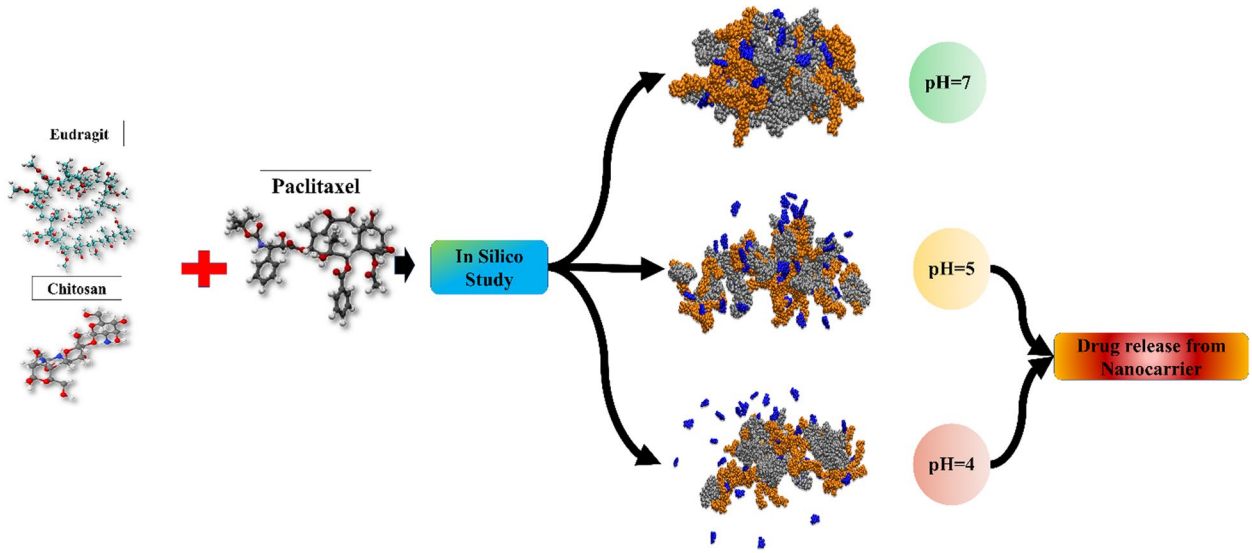

Introduction

The diverse physiological circumstances inside the human body serve as a catalyst for the development and exploration of nanocarriers with sophisticated physicochemical characteristics [1]. These nanocarriers are designed to overcome obstacles and barriers, allowing them to effectively target and treat specific areas affected by illnesses [2]. To this end, researchers examined various strategies and methods. From an experimental point of view, drug carriers are designed and synthesized based on the target's condition and evaluated their performance in vitro and in vivo [3, 4]. For instance, nanoparticles (NPs) with controlled properties (e.g., size, size distribution, electrical potential, etc.) and morphology (e.g., geometry, crystallinity, etc.) via different synthesis methods (e.g., self-assembly, crosslinking, and in-situ polymerization) have been tested for the efficacy of multiple products [5–7]. The wide applications of nanocarriers in biomedicine, including drug delivery, cancer therapy, immunotherapy, wound dressing, tissue regeneration, and etc., accelerate the development of multiple materials and synthesizing methods for nanoparticles and novel frameworks [8–10].

Chitosan, a natural biological and cationic polysaccharide mainly derived from marine crustaceans, is thought to be a promising nanomaterial with multiple medicinal uses [11]. Due to its biocompatibility, biodegradability, low toxicity, hydrophilicity, and structural diversity, it is an appropriate and viable drug delivery carrier for treatments and diagnostics [12, 13]. Internal enzymes such as lysozymes and chitosanases may breakdown chitosan to get oligosaccharides and monosaccharides, which can then be absorbed by the body [11].

However, chitosan has not been widely used in the clinic despite its unique physicochemical and biological features, owing to its limited solubility and poor mechanical properties [14]. To address these challenges, numerous ways of altering and improving its performance have been devised [14]. Based on its strong affinity for functional proteins and capacity to self-assemble, free amino and hydroxyl groups have been used to build a diverse spectrum of chitosan derivatives with increased solubility [15]. As a result, chitosan has been extensively used in a variety of biomedical and pharmaceutical studies, including drug [16], gene [17], and vaccine [18] delivery, regenerative medicine [19], and tissue engineering [20] concepts, along with wound healing [21] and cosmetic product manufacturing [22]. Chitosan-conjugated components in targeted tumors also react to external or internal physical and chemical stimuli, referred to as environment triggers [23].

Polymethacrylate polymers for pharmaceutical applications, often known as Eudragit, are synthetic polymers with a methacrylate monomer ratio ranging from two to three, such as methacrylic acid, methacrylic acid esters, and dimethylaminoethyl methacrylate [24]. Eudragit polymers are classified as cationic, anionic, or neutral and are available as powders, granules, aqueous dispersions, and organic solutions [25]. The Eudragit family has the same common structure, but differs in their substituents, which give diverse chemical characteristics.

Due to their pH-dependent water solubility, these polymers are ideal coating agents for drug delivery systems [26]. Furthermore, the solubility of these polymers in a range of organic solvents, which are utilized in the solvent evaporation technique, is a significant benefit in the development of pharmaceutical technology to increase pharmaceuticals solubility [27].

Even with polymeric nanocarriers, bioavailability and drug release at the disease site remain uncontrolled [28]. To address this issue, several effective approaches have been investigated for synthesizing polymeric nanocarriers possessing characteristics that respond to stimuli such as redox potential, temperature, pH, and light have been established [29–31]. Because of their capacity to improve bioavailability at the disease site, the resulting stimuli-responsive polymeric nanocarriers have shown great promise in drug delivery applications [32]. In such systems, drug release is regulated in response to external or endogenous stimuli [33, 34]. Besides, molecular structure is critical in responding to stimuli.

The study of macromolecular structure is crucial to understanding biology [35]. The basis of biological activity is molecular interactions, which are the product of macromolecular structures [36]. Prior to taking any practical activity, it is preferable to do a mathematical calculation and research. Molecular dynamics (MD) simulations have evolved into a sophisticated method for understanding macromolecular structure–function relationships [37]. To achieve a better understanding of intra/intermolecular interactions, the agents under consideration are extensively examined on an atomic scale [38, 39]. Simulation process timeframes are comparable to physiologically relevant timeframes. The information given on dynamic macromolecule properties is strong enough to shift the conventional paradigm of structural bioinformatics from single structure study to conformational ensemble analysis [37, 40]. MD simulation, which is capable of modeling and analyzing numerous macromolecules such as drugs and polymers, allows for the discussion of prospective treatment methods for a variety of medical concepts.

Running MD simulations are possible through various techniques. All-atom molecular dynamics (AA-MD) simulation, in which each atom is represented individually, is more precise but computationally costly and is normally used only for brief simulations of up to a few microseconds and smaller systems in length [41]. AA-MD simulation has been shown to be an effective method for understanding the structure and dynamics of soluble proteins, lipid bilayers, and polymers [42]. However, the computational complexity of explicitly modeling every atom of the solute and solvent restricts AA-MD simulations to tens of nanosecond timescales. To address this limitation, coarse-grained molecular dynamics (CG-MD) force fields were created, in which groups of atoms are represented by a single CG-MD bead [43]. The CG-MD technique is a strategy for running longer simulations, using larger boxes during simulation. Although the CG-MD model loses the accuracy of the AA-MD model by representing 3–4 heavy atoms with a single bead, its advantage is that it allows for longer simulations [43].

The aim of the current work is to gain a deeper understanding of molecular interactions and the mechanism of PAX drug adsorption and release from the Chitosan-Eudragit carrier. For this purpose, molecular simulation has been used in different dimensions to investigate the molecular interactions of this drug delivery system. This study exhibits the pH-dependent drug release mechanism for Chitosan-Eudragit nanoparticles via AA-MD and CG-MD techniques. In this regard, delivering antitumor drug, Paclitaxel (PAX), through employing Chitosan-Eudragit nanocarriers were investigated. To the best of our knowledge, this is the first in-silico study to demonstrate the pH-dependent drug release mechanism for Chitosan-Eudragit nanoparticles, confirmed by previous experimental works.

Results and disscusions

The structures of Chitosan and Eudragit used for MD simulations are shown in Fig. 1a. Results from both AA-MD and CG-MD simulations have been compared with experimental data for initial evaluations. Figure 1b exhibits PAX release (%) from computational approaches with experimental results. Interestingly, computational and experimental results are in appropriate agreement. In a comprehensive view, both mathematical approaches can catch the trend in the release diagram vs. pH conditions and anticipate comparable data to the reported real numbers. AA-MD results are lower than experimental data in all pH conditions, while CG-MD predicts more than experimental release. However, considering the trend of release values, the differences between computed and reported data are negligible.

Furthermore, to validate computational results with reported experimental data, the formation of NPs through hydrodynamic radius (R_h) and the radius of gyration (R_g) obtained through simulations were compared (Fig. 1c). The R_g resembles the self-assembly of polymeric chains in the lab condition throughout the simulation. Moreover, R_g can be interpreted as the stability of the NPs' model, i.e., the less the R_g size indicates the tighter and more stable particle. In this line, the diagrams showing the R_g change over the simulation time (in nanosecond scale) were prepared to be compared with the hydrodynamic size of NPs in the lab that has been prepared in the various reaction periods (based on hour

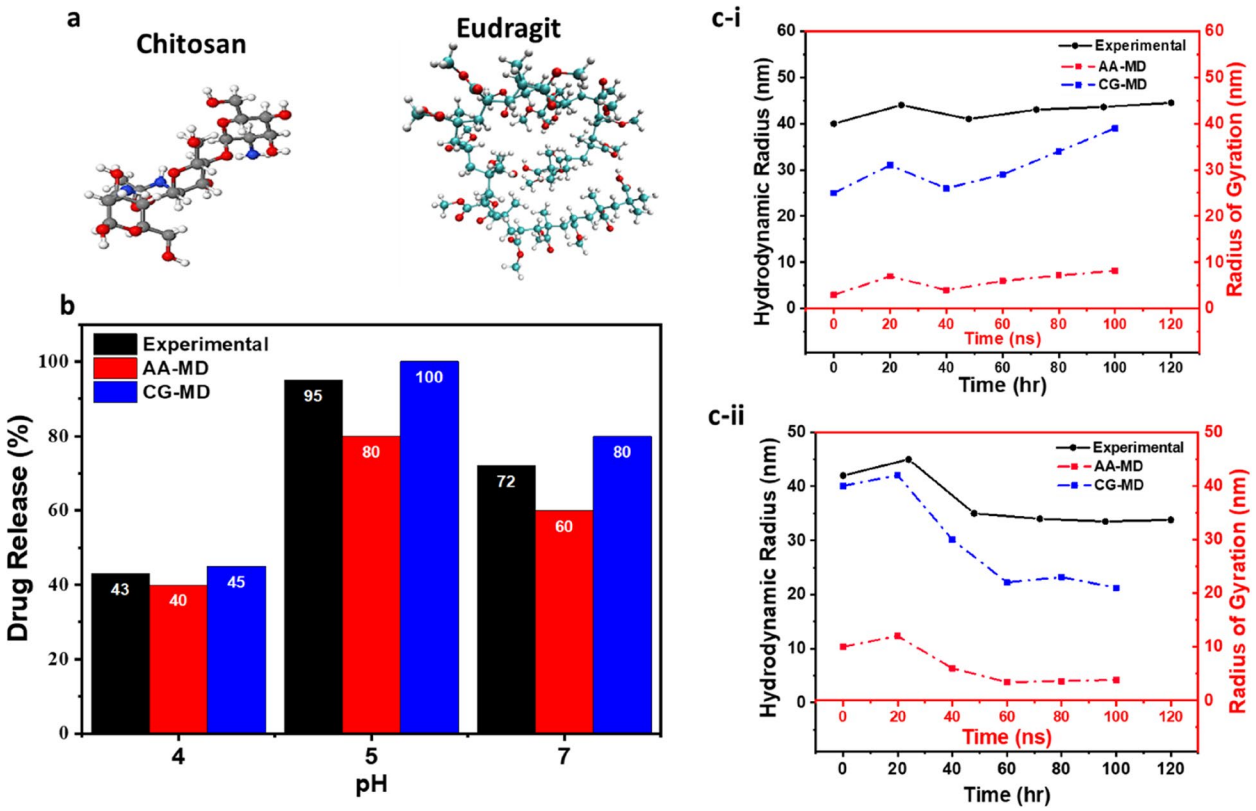

Fig. 1 Initial comparison of the computational approaches with reported real data of PAX-Citosan-Eudragit. **a** molecular structure of Chitosan and Eudragit used in simulations. **b** Drug release (%) in varying pH conditions for real and mathematical methods (AA-MD and CG-MD). **c** i,ii) Comparison between hydrodynamic radius (R_h) of NPs (with different reaction times) with radius of gyration (R_g) (during simulations) obtained from computational methods at pH = 5 and 7, respectively. All diagrams are in good agreement with eachother, i.e., simulations anticipate the variation of R_g similar to the size of NPs. Experimental data was obtained from [44]

scale). The change in R_g vs. AA-MD and CG-MD simulation times resembles the change in the size of actual NPs vs. reaction times. Altogether, the agreements between R_g and R_h, in addition to the release results, provide other pieces of evidence on the reliability of the computational procedures and approaches to continue for further investigations.

The interaction of the Chitosan molecule with the PAX molecule is simulated at different pHs. Gyration radius and energy analysis, charge distribution, the RDF and SASA diagrams are supposed to illustrate the results of this computational study. These results are obtained from both AA-MD and CG-MD simulations. The results of a comparison of analyses show PAX adsorption and release at specific pH levels.

Validation of simulations with experimental results

Figure 2 shows the release of PAX employing nanocarrier via simulation methods of AA-MD and CG-MD. The simulation results show a similar release percentage with the results of the experimental work. Experimental data was obtained from a previously published research by Hasani-Sadrabadi et al. [44], in which they assessed various pH conditions on PAX delivery through multiple nanocarriers. Consistency of the simulation and experimental work results demonstrates the validity of the method and algorithm used in this work.

Figure 3 illustrates the changes in nanocarrier size during simulation by AA-MD and CG-MD methods in blue and purple, respectively. Also, the nanocarrier size of the experimental work is shown in red. The process of altering nanocarrier size in computational and experimental work is similar. This result shows the accuracy of the methods and algorithms used in this work.

Table 1 shows the average energy obtained from the simulation in the canonical (NVT) ensemble stage, and the experimental work. The average energy similarity in the NVT phase shows the accuracy of the methods and algorithms used in this work. At the NVT stage, the number of moles, temperature, and volume of the simulation box are fixed during the simulation. Molecular simulations are very sensitive to the force-field and potential

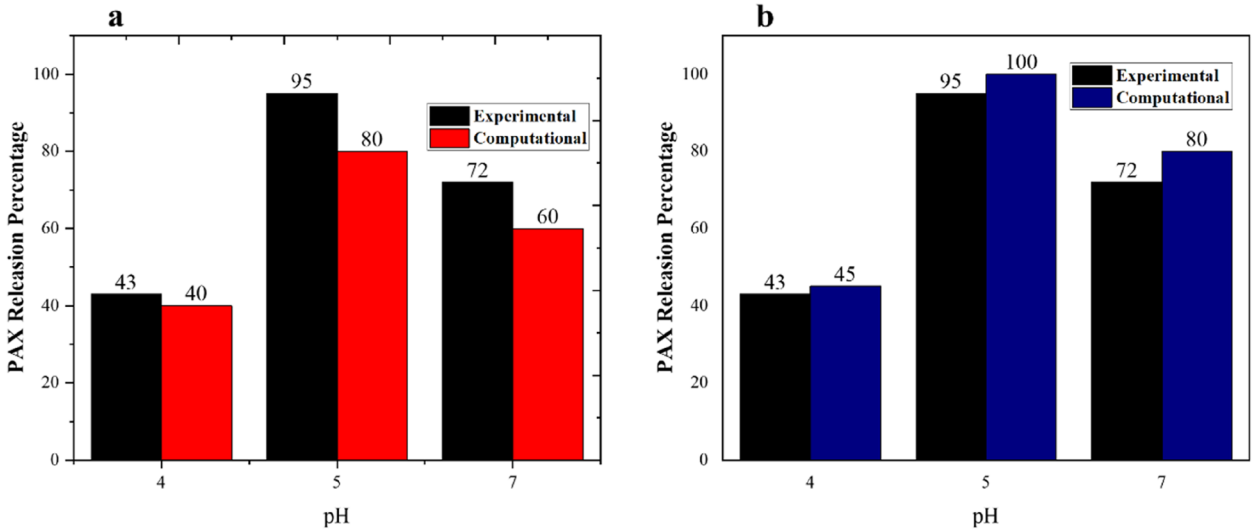

Fig. 2 The comparison of PAX release (%) by nanocarrier through (**a**) AA-MD, and (**b**) CG-MD simulation methods. Experimental data was obtained from [44]

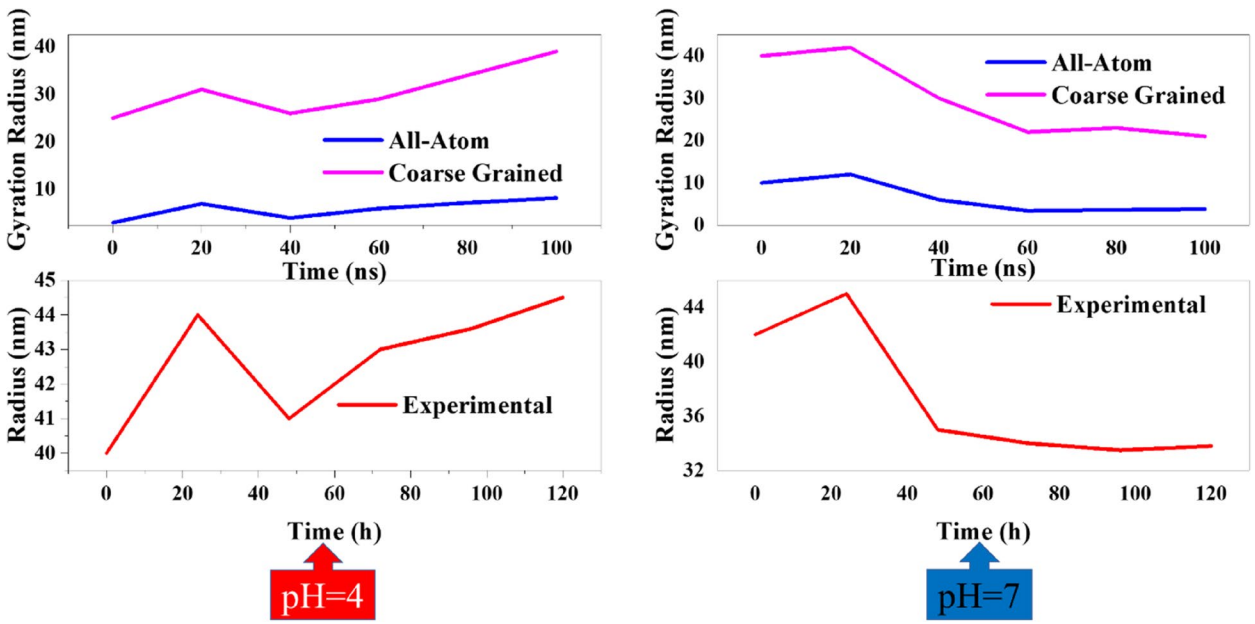

Fig. 3 The comparison among nanocarrier size resulted from computational and experimental works

Table 1 The average energy obtained from the simulation in the NVT stage and the experimental situation. Experimental data (reference simulation) was obtained from [44]

Simulation	Energy (Kj/mol)
Refrence Simulation	1988.73
All-Atom Simulation	2468.148
Coarse Grained Simulation	1979.528

functions. The potential function that the reference simulation used is different from the potential function of all-atom simulation. This caused a difference in the results as shown in Table 1. In coarse-grained simulations, this difference is much less (less than one percent). Given that molecular simulations have many limitations in terms of dimensions, potential functions, assumptions, etc., more in qualitative studies and are semi-quantitative, so the

differences are usual in molecular simulations as long as they do not cause conflict in the trends and the qualitative understanding of the subjects.

AA-MD simulation

In AA-MD simulation, the results are presented on smaller scales but more accurately. The first analysis is the charge distribution analysis, which shows the charge density along with the simulation box (with Coulomb/box volume unit) and is made for PAX molecules, Chitosan, and Eudragit monomers (Fig. 4). Figure 4a shows the charge distribution for the Eudragit monomer. In this monomer, positive–negative charges are seen in proportion, considering that the ratio of negative charges is more than positive charges, and the charge of this polymer is negative. Also, as shown in Fig. 4b, Chitosan monomer has different charge distributions. In this monomer, there are positive and negative charges, where the positive charge is due to the presence of the amine group, and the negative charge is linked to the presence of the OH group. According to Fig. 4c, the PAX molecule has a relatively negative charge, and this is due to the OH group being in its structure. Also, the binding of PAX and nanocarrier after simulation is shown in Fig. 4d.

Figure 5 also shows the energy diagrams and the number of hydrogen bonds for the PAX molecule and the Eudragit and Chitosan polymers at different pHs. The energy diagram is calculated based on the electrostatic van der Waals energy and the total energy. The van der Waals energy results from the interaction among the molecules, based on the Leonard Jones equation [45]. Regarding this equation and based on the various molecules and atoms' mass, van der Walls energy calculations are obtained. Electrostatic energy is also calculated depending on each atom's charge, derived from Coulomb's law [46]. In AA-MD simulation, each atom has charge and mass and based on these two parameters, van der Waals and electrostatic energies are calculated. The total energy is obtained regarding the sum of van der Waals and electrostatic energies. Energy analysis is essential in pH-dependent simulations since with the change of pH, both the charge of the atoms and the number of

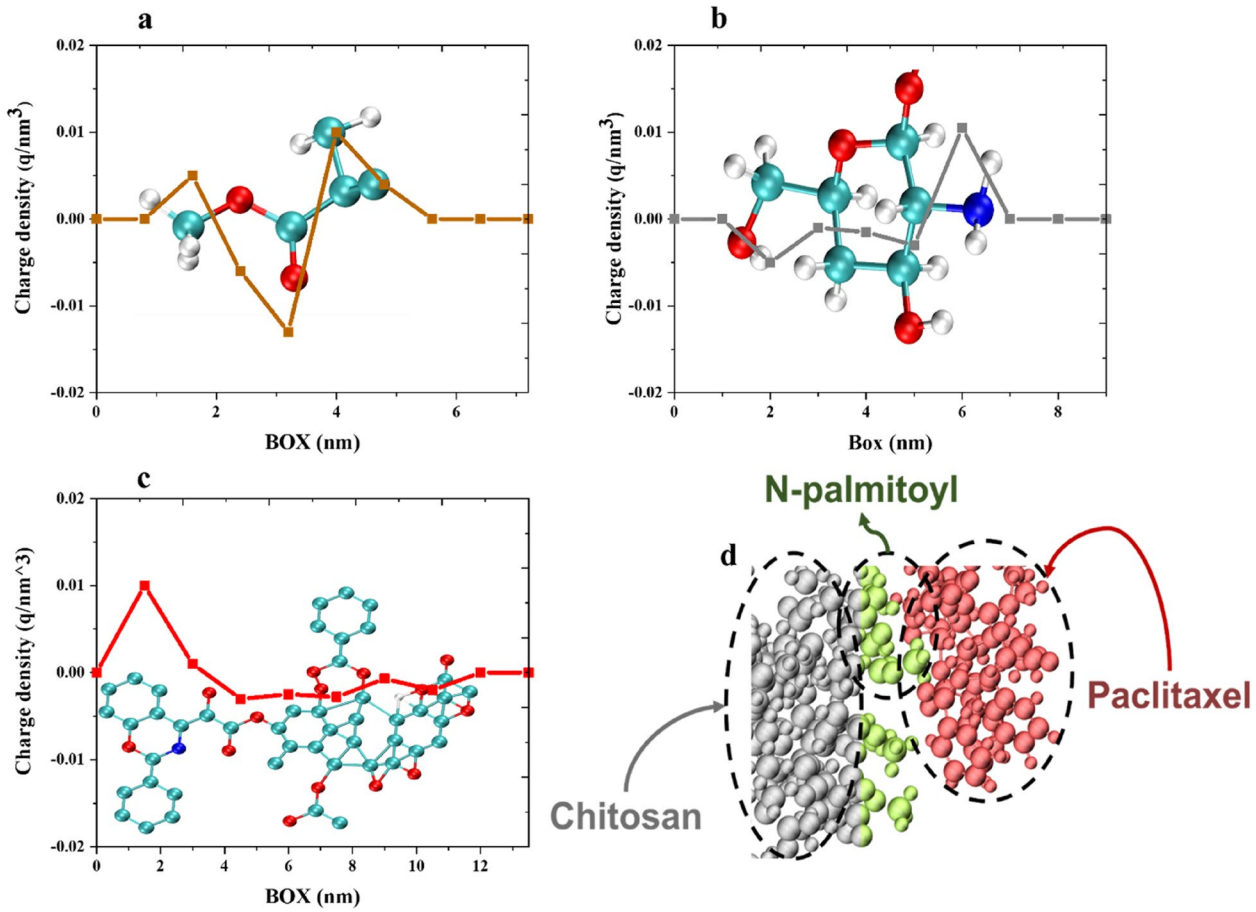

Fig. 4 Charge distribution in the structure of molecules (**a**) Eudragit, (**b**) Chitosan, (**c**) PAX, and (**d**) Binding of PAX molecules and nanocarrier after simulation

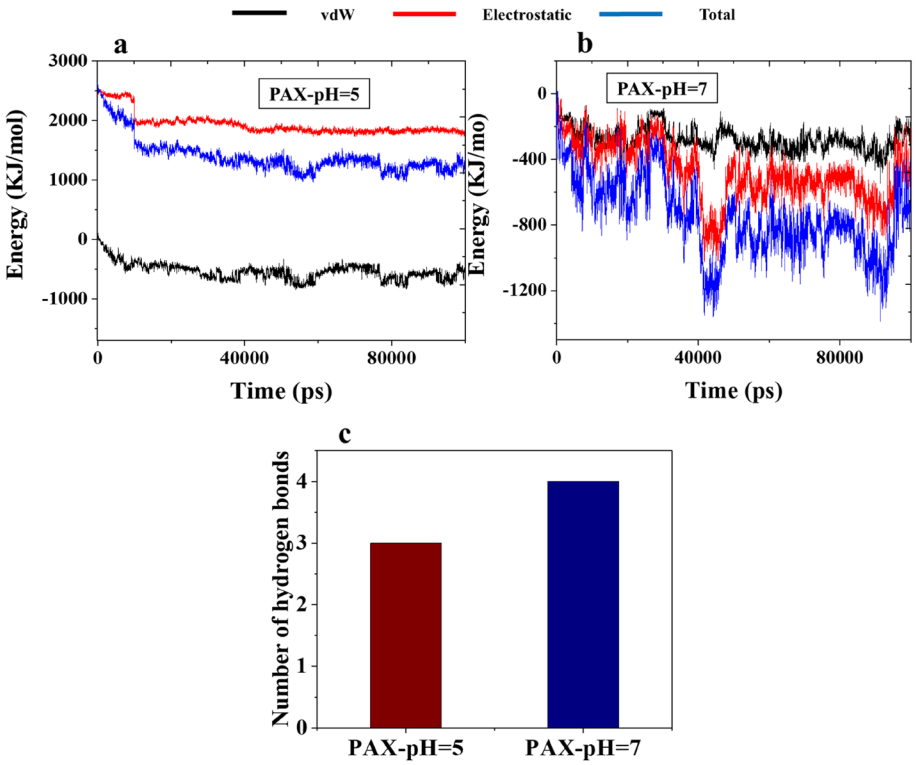

Fig. 5 Energy diagram of the interactions among PAX and nanocarrier over time at (**a**) pH = 5; and (**b**) pH = 7; (**c**) hydrogen bonds formed between PAX and nanocarrier at pH = 5 and pH = 7

hydrogens and proteins in the system change. The charge alter causes immediate changes in electrostatic and total energy and consequently affects van der Waals energy.

The diagrams in Fig. 5 demonstrate that with the acidification of the system, the number of protons has also increased; hence its electrostatic energy has become positive. At the pH = 7 (neutral), the average total energy is approximately -800, while at the pH = 5, the number of protons increases, and the charge becomes positive, and the average total energy is about 1500. However, van der Waals energy, which depends on atoms mass, has changed very quitely. These results indicate that at neutral pH, PAX adsorption occurred through Chitosan and Eudragit nanocarriers, while at the acidic pH, PAX excretion would occur. Therefore, it could be concluded that the PAX excretion also takes place at the acidic pH of the cancerous tumor. Another analysis that is essential in pH-dependent simulations is the analysis of hydrogen bonds, which are more potent than van der Waals and electrostatic energies. pH changes are evident in Fig. 5c as the number of hydrogen bonds increases in terms of simulation time. Also, protonation depends on pH changes.

The number of hydrogen bonds established at neutral pH is greater than the number of hydrogen bonds established at acidic pH. According to the Arrhenius theory [47], the lower average of hydrogen bonding at acidic pH indicates that nanocarrier and drug molecules release themselves in the hydrogen environment in cancer cells' acidic conditions. This phenomenon resulted in positive electrostatic energy in Fig. 5a and the number of hydrogen bonds in Fig. 5c. Thus, at acidic pH, not only do the molecules gain the same charge, but also, they lose their hydrogen to form a hydrogen bond, resulting in the excretion of PAX molecules from the nanocarrier. Figure 5c shows that the average hydrogen bond increases slightly by 40 ns. This point indicates that from 40 ns onwards, the adsorption of PAX molecules into the nanocarrier increases and the drug bind to the nanocarrier.

Figure 6 shows the radial distribution function (RDF) diagram and the gyration radius. The RDF diagram depicts the distribution of PAX loads around the nanocarrier at different pHs. The maximum of this graph shows the highest adsorption rate among PAX and nanocarrier molecules. As shown in Fig. 6a, PAX molecules were more adsorbed at neutral pH. It can also be seen that at more than 2 nm distances, the number of PAX molecules is less at neutral pH. In general, this diagram shows that the PAX molecules were more around the nanocarrier molecules at neutral pH than at the acidic pH.

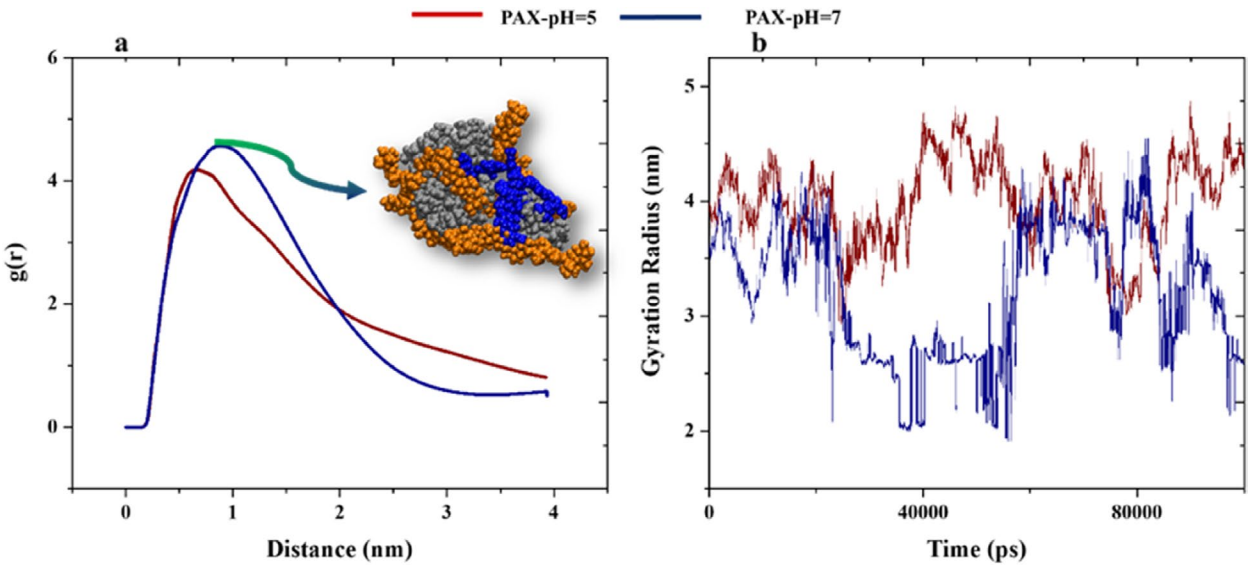

Fig. 6 Analyzing the RDF (g(r)) and the gyration radius (**a**) Density of PAX around the nanocarrier at pH = 5 and 7; (**b**) Gyration radious change of PAX over time at pH = 5 and 7

Figure 6b also shows the gyration radius, which indicates the radius of the accumulated molecules at various simulation times. According to this diagram, PAX molecules and nanocarriers have accumulated more at neutral pH. This diagram shows that the mean gyration radius and its endpoint at neutral pH were less than at acidic pH. The simulation outputs indicate that PAX molecules are more adsorbed at neutral pH.

Figure 7 demonstrates the information based on the analysis of solvent accessible surface area (SASA). Figure 7a shows the available water area in PAX molecules. PAX molecules were more in contact with water at an acidic pH. Also, the continuous decrease of this diagram at neutral pH shows that PAX molecules at neutral pH were constantly adsorbed to the nanocarrier, while in the acidic state, several fluctuations are seen in the diagram; these fluctuations can be due to the formation of electrostatic repulsion in the acidic state.

Figure 7b also shows the changes in the contact surface between nanocarriers and PAX molecules over time. These changes were compared to the initial simulation mode, which is why the value of this parameter was 0 in the 0-ns mode. The contact area indicates that the surface in contact among the drug molecules and the nanocarrier in the neutral state is nearly twice that of the contact surface among the nanocarrier molecules and the drug in the acidic state. As a result, PAX molecules adsorb in the neutral state was much higher.

Figure 8 also shows the root-mean-square deviation (RMSD) and root-mean-square fluctuation (RMSF) diagrams. These diagrams illustrate the oscillations of the system (separatly for each atom) in terms of time. At the beginning of the simulation, fluctuations are high, while they decrease at the end of the simulation. This trend indicates that the system is moving towards stability. That is, the energy level of the molecules decreases during simulation time. Table 2 also shows the mean, maximum and minimum values of RMSD and RMSF.

Figure 8b and Table 2 show that the mean RMSD at neutral pH was lower than the acidic state, and even the range of fluctuations among maximum and minimum RMSD at neutral pH was smaller than acidic pH. The RMSF analysis also reports the same results for each atom in Fig. 8b and Table 2. According to this analysis, the average fluctuations for all atoms at all time intervals in the neutral pH state were less than in the acidic state. Moreover, Table 2 states that the maximum and minimum fluctuations of RMSF at neutral pH were less than at acidic pH. In addition to showing that the system and the simulation are moving towards a steady state, these analyses also show that this level of stability is better in the neutral state than in the acidic state, and the system is more stable in the neutral state.

The SASA analysis for the Edragit monomer is reported in Fig. 9a. In this analysis, the contact surface of various parts of the monomer with water is shown in color. The range of this contact surface is between 1.03 and 2.34 nm. In the acidic state, the contact surface tends to be more towards 2.34 nm. This means that in the acidic state, the molecules were more inclined to water, and they were able to put more of their surface in contact with water. According to the Arrhenius theory [47], when free

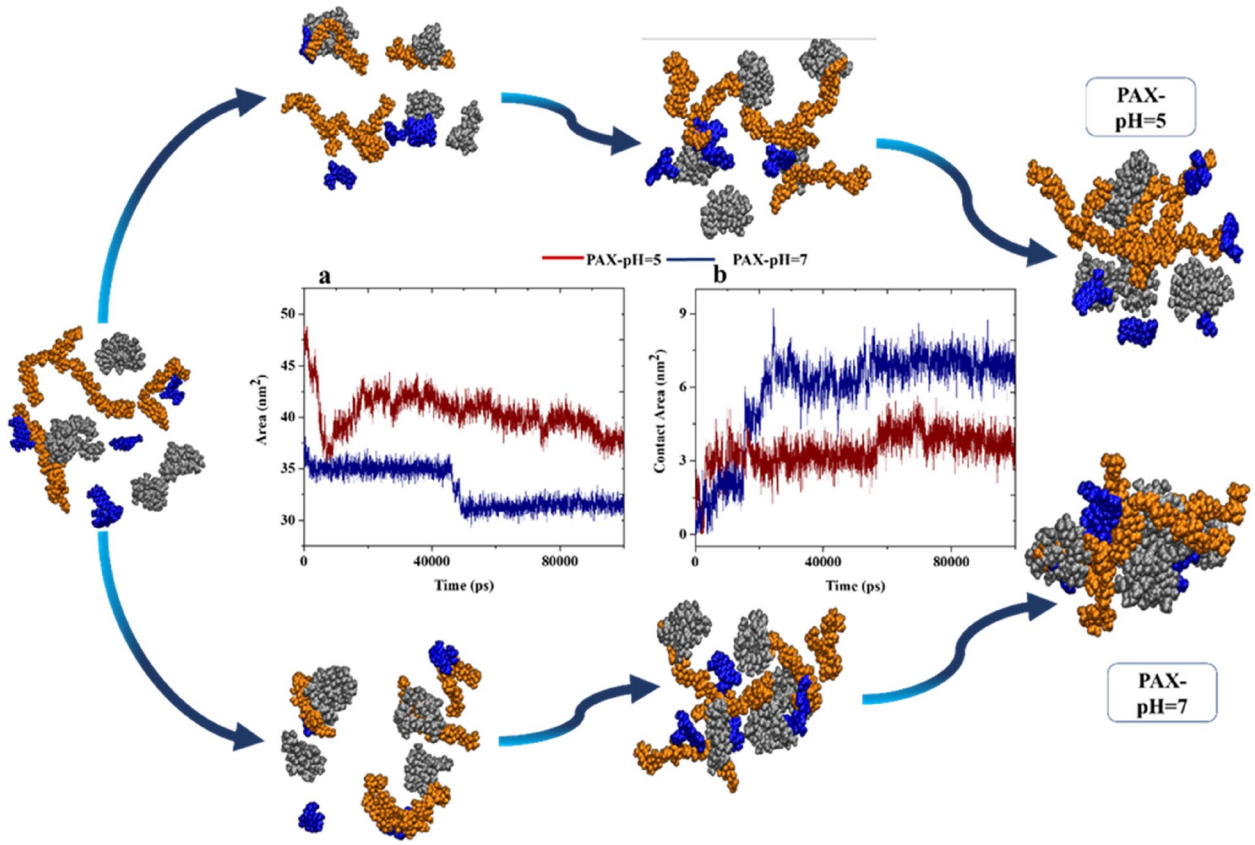

Fig. 7 SASA analysis results. **a** Contact area changes among PAX and water when interacting with the nanocarrier; and (**b**) Contact surface changes among nanocarrier particles at pH = 5 and pH = 7

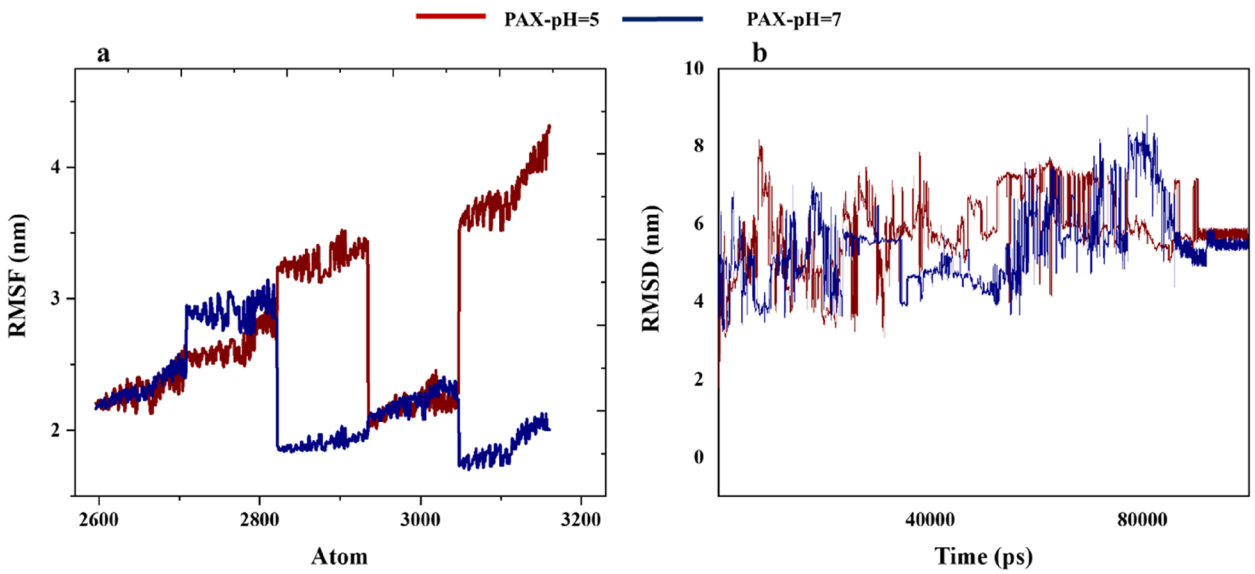

Fig. 8 The RMSF and RMSD analysis results. **a** Fluctuations of PAX atoms upon interacting with the nanocarrier at pH = 5 and pH = 7; (**b**) fluctuations of PAX particles over time at pH = 5 and pH = 7

Table 2 The mean, maximum and minimum RMSD and RMSF values for PAX

	RMSF (nm)		RMSD (nm)	
	pH = 5	pH = 7	pH = 5	pH = 7
Average	2.848078761	2.247470796	6.28327302	5.418648217
Maximum	4.317	3.1406	9.1452227	8.8004856
Minimum	2.0164	1.7036	0.0000232	0.0002312

hydrogen is released in the acidic state, a charge difference is created between the molecule and water, and they become electrostatically inclined to absorb each other. However, in the neutral state, where the adsorption of water molecules is almost negligible, these monomers are in contact with other molecules. This means that these molecules may have been in contact with PAX, and more adsorption may have occurred.

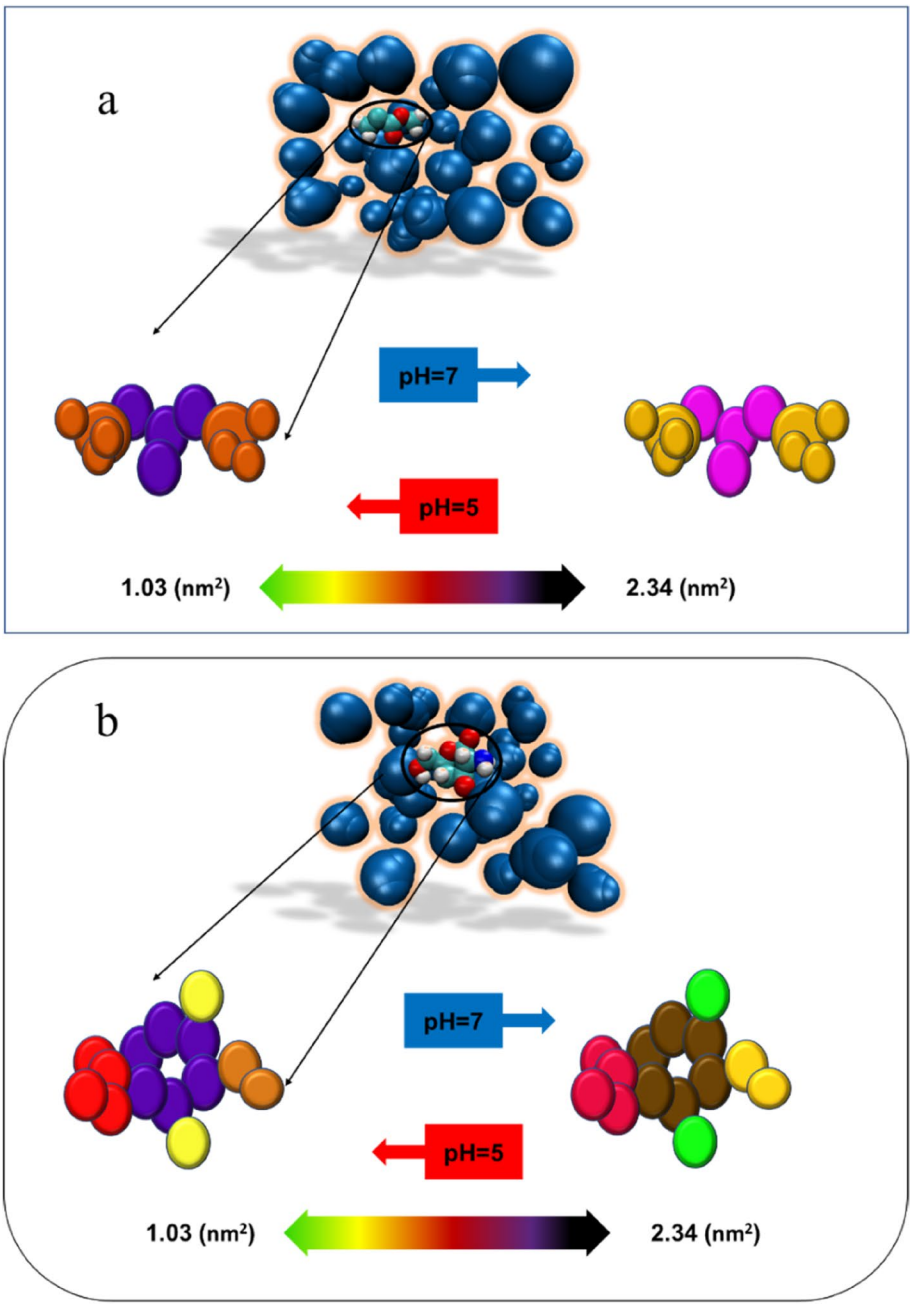

Fig. 9 SASA analysis results of Edragit and Chitosan monomers. **a** Changes in contact surface of Eudragit and water monomer atoms at pH = 5 and pH = 7 (**b**) Contact surface changes of Chitosan and water monomer atoms at pH = 5 and pH = 7

Figure 9b shows the same analyses for the Chitosan monomer. A greater tendency to absorb water could be seen in the acidic state. There is a strong tendency for water to be absorbed by the aromatic ring within the Chitosan monomer in both acidic and alkaline states. This tendency has reached its maximum in the acidic state (2.34 nm). In this case, less adsorption in the acidic state and more in the neutral state could be concluded.

CG-MD simulation

In addition to the AA-MD simulation method, CG-MD simulations have also been performed. These simulations were performed on larger scales and with more molecules than in the AA-MD simulation state. Figure 10 shows the energy diagrams obtained from these analyses. The results of these graphs are pretty similar to the results obtained in the AA-MD method. According to these results, adsorption occurs at neutral and acidic pH, and electrostatic energy causes repulsion among molecules.

Figure 11 also shows gyration radius and SASA diagrams. The gyration radius in these diagrams is in higher range than in the AA-MD method, while fully confirming the results of that analysis. The result of analysis of the gyration radius indicates that accumulation occurred in the neutral state. The results are also evident in Fig. 11b, which is related to the SASA diagram. The result of SASA analysis in the CG-MD simulation method also dictates PAX adsorption in the neutral state. Based on these results, at neutral pH, the PAX molecules had a lower contact surface with water, meaning that these molecules were attached to the nanocarrier and did not float in water. The simulation snapshots can be seen in Fig. 11 since the scale of the molecules in the CG-MD mode is partially out of the nano mode, and the molecules interact in the micro mode, and their large number and dispersion are visible.

Figure 11c also shows the contact surface among PAX and nanocarriers. According to this diagram, the contact surface among drugs and nanocarriers increases at neutral pH. This contact surface is constant at acidic pH and does not change much during the simulation. Also, repulsions are side by side during simulation.

Conclusions

The current study presents the pH-dependent anti-tumor drug release mechanism employing Chitosan-Eudragit bioresponsive nanocarriers through an experimental and MD study. Multiple effective parameters for the nanocarrier-drug interaction stability have been studied. Results showed that the process of changing the size of nanocarriers during simulation is identical in computational and experimental works. PAX adsorption occurred through Chitosan-Eudragit nanocarriers at neutral pH, while PAX excretion occurred at acidic pH. As a result, it is possible to deduce that PAX excretion occurs at the acidic pH of the cancerous tumor. The amount of hydrogen bonds formed at neutral pH is more than the number formed at acidic pH. The decreased average of hydrogen bonding at acidic pH shows that nanocarrier and drug molecules release themselves in the hydrogen environment in acidic cancer cells. At acidic pH, the molecules not only receive the same charge, but they also lose their hydrogen

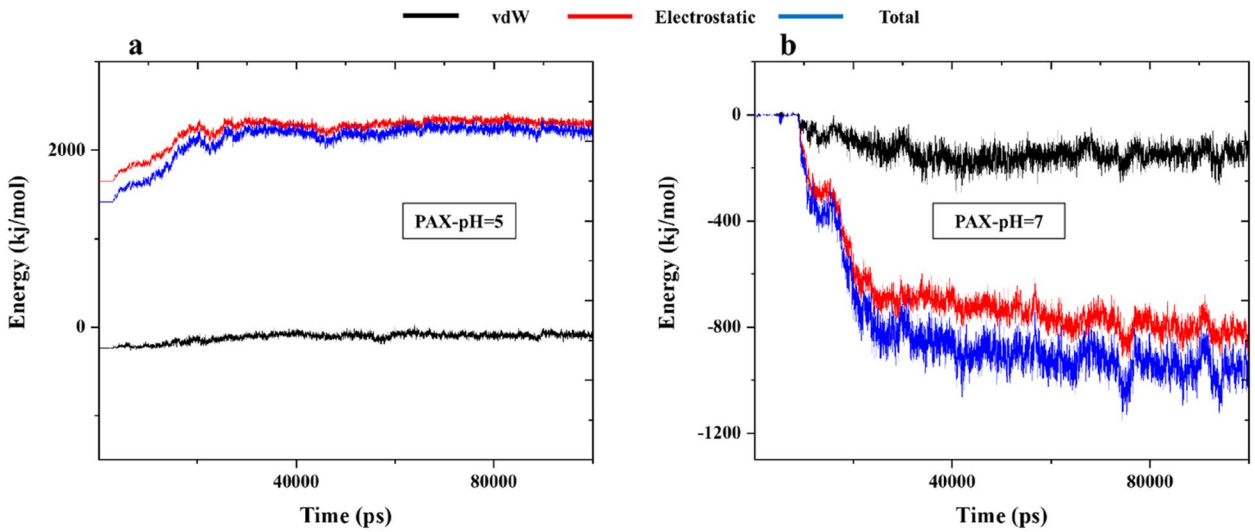

Fig. 10 Graph of energy resulting from interactions among PAX and nanocarrier over time at (**a**) pH = 5, and (**b**) pH = 7 through CG-MD simulation method

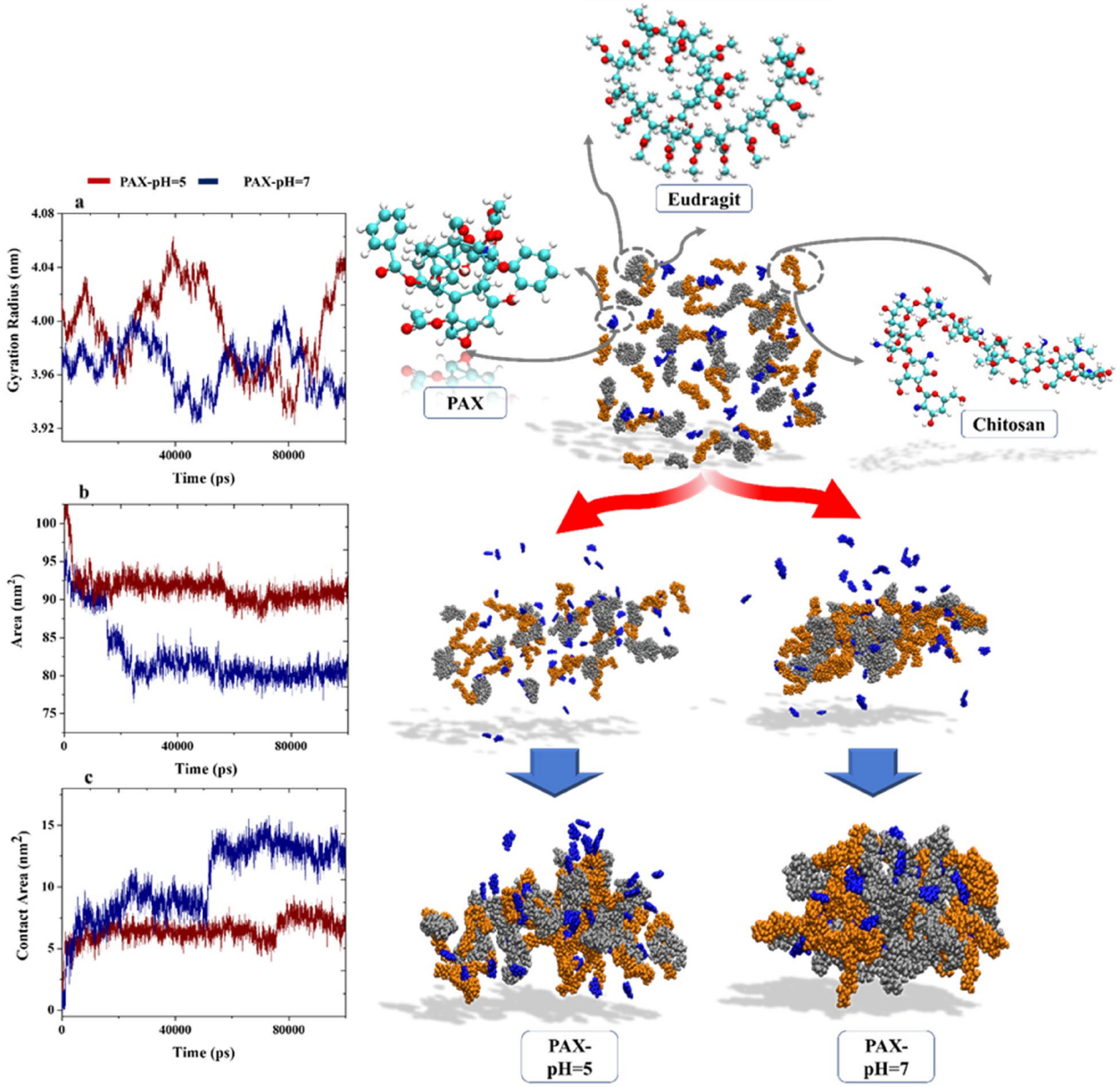

Fig. 11 Results of gyration radius and SASA analysis through CG-MD simulation (**a**) Changes in the PAX drug gyration radius over time at pH = 5 and pH = 7; (**b**) PAX and water contact surface changes upon interacting with nanocarrier at pH = 5 and pH = 7; (**c**) Contact surface changes among nanocarrier particles at pH = 5 and pH = 7

to form a hydrogen bond, leading to the excretion of PAX molecules from the nanocarrier.

The results of the gyration radius reveal that the PAX molecules were more adsorbed at neutral pH. The contact area demonstrates that the surface in contact between the drug molecules and the nanocarrier in the neutral state is roughly twice as large as the surface in contact between the drug molecules and the nanocarrier in the acidic state. Consequently, the adsorption of PAX molecules in the neutral state was significantly increased. The maximum and lowest RMSF variations at neutral pH were fewer than those at acidic pH. In addition to the system and simulation approaching a steady-state, these analyses reveal that this degree of stability is better in the neutral state than in the acidic state, and the system is more stable in the neutral state. The used Chitosan-Eudragit bioresponsive nanocarriers have a relatively stable structure at higher pH but deform and release their payloads at lower pH. Considering the biocompatibility and adjustability of Chitosan-Eudragit bioresponsive nanocarriers for PAX drug delivery, it seems

that this work can be studied further. In-vitro and in-vivo studies can complete and deepen the current work results. The use of advanced methods and new improvements in the microfluidic synthesis of Chitosan-Eudragit carriers and the testing them in the living environment can be a good suggestion for future research works. So far, based on the results obtained from molecular simulation, it can be predicted that chitosan carriers will probably be able to play a key role in the delivery of anticancer drugs, especially PAX, in the future of cancer treatment. Of course, proving this prediction to the extent that it can be used clinically requires additional research at different levels.

Materials and methods

Molecule designs

The molecular structure of polymers and PAX are designed using Gaussian, and then the structures are geometry-optimized with Avogadro and Hyperchem software. Afterward, the leading optimization was performed with Gaussian based on the ONIOM method consisting of three layers. The Gaussian 09 software with the ONIOM method is employed to optimize (based on DFT and semi-empirical methods) the structures in three layers: high (b3lyp and basis set of 6–311 + G*), medium (b3lyp and basis set of STO-3G) and low (PM6). Charge density has been calculated by Gaussian, which is used in the topology parameters. Molecular topologies were retrieved from the PolyParGen web interface. Next, the leading optimization is carried out in simulation cells 6 × 6 × 20 nm3 for 50 ns for each molecule.

Simulation

The primary simulation was performed with GROMACS 2020 at MD, NPT (constant number of atoms, N; constant pressure, P; constant temperature, T), NVT (constant number of atoms, N; constant volume, V; constant temperature, T), and EM steps. Simulation boxes are considered 10 × 10 × 10 nm3 with an OPLS-AA force field. The NPT and NVT were performed for 0.5 ns (with 1 femtosecond time steps) with isotropic Berendsen algorithm at 1 bar and velocity-scaling algorithm at 300 K, respectively. The MD (100 ns with 2 fs time step) simulations. The cut-off radius was adjusted at 1.2 nm for the van der Waals and Coulomb interactions. The pressure and temperature algorithms are isotropic Parrinello–Rahman algorithm at 1 bar and with nose–hoover (velocity-scaling algorithm in NVT and NPT) at 300 K. We used coulomb energy algorithm and Particle Mesh Ewald (PME). The Coarse-Grained simulations were performed at different pH conditions with the Martini force field in the simulation cells 40 × 40 × 40 nm3 for 100 ns (with 30 fs time step).

Abbreviations

AA-MD	All-atom molecular dynamics
CG-MD	Coarse-grained molecular dynamics
MD	Molecular dynamics
NPs	Nanoparticles
PAX	Paclitaxel
PME	Particle Mesh Ewald
RDF	Radial distribution function
RMSD	Root-Mean-Square Deviation
RMSF	Root-Mean-Square Fluctuation
SASA	Solvent Accessible Surface Area
VDW	Van der Waals

Acknowledgements
Not applicable.

Authors' contributions
All authors contributed to the investigation, conceptualization, and analysis, and were involved in the writing process.

Funding
This work was funded by Deputy for Research and Technology, Tabriz University.
of Medical Sciences [grant number: 74044].

Availability of data and materials
The data that support the findings of this study are available from the corresponding author upon reasonable request.

Data availability
The data that support the findings of this study are available from the corresponding author upon reasonable request.

Declarations

Ethics approval and consent to participate
Ethics code: IR.TBZMED.VCR.REC.1403.103.

Consent for publication
Not applicable.

Competing interests
The authors declare no competing interests.

Author details
[1]Department of Chemical Technologies, Iranian Research Organization for Science and Technology (IROST), P.O. Box 33535111, Tehran, Iran. [2]Department of Chemical Engineering, Amirkabir University of Technology, 424 Hafez Avenue, Tehran, Iran. [3]Chemical Engineering Department, Urmia University of Technology, Urmia 57166-419, Iran. [4]Department of Tissue Engineering, Faculty of Advanced Medical Sciences, Tabriz University of Medical Sciences, Tabriz, Iran. [5]Regenerative Medicine Group (REMED), Universal Scientific Education and Research Network (USERN), Tehran, Iran.

Received: 25 January 2024 Accepted: 26 August 2024
Published online: 09 September 2024

References

1. Yu Y, Wang L, Ni S, Li D, Liu J, Chu HY, Zhang N, Sun M, Li N, Ren Q, Zhuo Z, Zhong C, Xie D, Li Y, Zhang Z-K, Zhang H, Li M, Zhang Z, Chen L, Pan X, Xia W, Zhang S, Lu A, Zhang B-T, Zhang G. Targeting loop3 of sclerostin preserves its cardiovascular protective action and promotes bone formation. J Nat Commun. 2022;13(1):4241.
2. Rizvi SAA, Saleh AM. Applications of nanoparticle systems in drug delivery technology. Saudi Pharm J. 2018;26(1):64–70.
3. Peng Y, Chen L, Ye S, Kang Y, Liu J, Zeng S, Yu L. Research and development of drug delivery systems based on drug transporter and nanoformulation. Asian J Pharm Sci. 2020;15(2):220–36.

4. Dai J, Ashrafizadeh M, Aref AR, Sethi G, Ertas YN. Peptide-functionalized, -assembled and -loaded nanoparticles in cancer therapy. J Drug Discov Today. 2024;29(7):103981.
5. Fu S, Sun Z, Huang P, Li Y, Hu N. Some basic aspects of polymer nanocomposites: A critical review. Nano Mater Sci. 2019;1(1):2–30.
6. Li B, Wang W, Zhao L, Li M, Yan D, Li X, Zhang J, Gao Q, Feng Y, Zheng J, Shu B, Yan Y, Wang J, Wang H, He L, Wu Y, Zhou S, Qin X, Chen W, Qiu K, Shen C, Wang D, Tang BZ, Liao Y. Aggregation-induced emission-based macrophage-like nanoparticles for targeted photothermal therapy and virus transmission blockage in Monkeypox. J Adv Mater. 2024;36(9):2305378.
7. Seraji AA, Bajgholi AA. Dual role of nanoclay in the improvement of the in-situ nanofibrillar morphology in polypropylene/polybutylene terephthalate nanocomposites. J Ind Text. 2022;52. https://doi.org/10.1177/15280837221133570.
8. Tan T, Feng Y, Wang W, Wang R, Yin L, Zeng Y, Zeng Z, Xie T. Cabazitaxel-loaded human serum albumin nanoparticles combined with TGFβ-1 siRNA lipid nanoparticles for the treatment of paclitaxel-resistant non-small cell lung cancer. Cancer Nanotechnol. 2023;14(1):70.
9. Zhao C, Tang X, Chen X, Jiang Z. Multifaceted carbonized metal-organic frameworks synergize with immune checkpoint inhibitors for precision and augmented cuproptosis cancer therapy. ACS Nano. 2024;18(27):17852–68.
10. Zhao M, Kang M, Wang J, Yang R, Zhong X, Xie Q, Zhou S, Zhang Z, Zheng J, Zhang Y, Guo S, Lin W, Huang J, Guo G, Fu Y, Li B, Fan Z, Li X, Wang D, Chen X, Tang BZ, Liao Y. Stem cell-derived nanovesicles embedded in dual-layered hydrogel for programmed ROS regulation and comprehensive tissue regeneration in burn wound healing. Adv Mater. 2024:2401369. https://doi.org/10.1002/adma.202401369.
11. Ghaz-Jahanian MA, Abbaspour-Aghdam F, Anarjan N, Berenjian A, Jafarizadeh-Malmiri H. Application of chitosan-based nanocarriers in tumor-targeted drug delivery. J Mol Biotechnol. 2015;57(3):201–18.
12. Li J, Cai C, Li J, Li J, Li J, Sun T, Wang L, Wu H, Yu G. Chitosan-based nanomaterials for drug delivery. J Mol (Basel, Switzerland). 2018;23(10):2661.
13. Alimirzaei F, Vasheghani-Farahani E, Ghiaseddin A, Soleimani M, Najafigharavi Z. pH-Sensitive Chitosan Hydrogel with Instant Gelation for Myocardial Regeneration. J Tissue Sci Eng. 2017;8:1000212. https://doi.org/10.4172/2157-7552.1000212.
14. Potaś J, Szymańska E, Winnicka K. Challenges in developing of chitosan – Based polyelectrolyte complexes as a platform for mucosal and skin drug delivery. Eur Polym J. 2020;140:110020.
15. Argüelles-Monal WM, Lizardi-Mendoza J, Fernández-Quiroz D, Recillas-Mota MT, Montiel-Herrera M. Chitosan derivatives: introducing new functionalities with a controlled molecular architecture for innovative materials. Polymers. 2018;10(3):342.
16. Martínez-Martínez M, Rodríguez-Berna G, Gonzalez-Alvarez I, Hernández MJ, Corma A, Bermejo M, Merino V, Gonzalez-Alvarez M. Ionic hydrogel based on chitosan cross-linked with 6-phosphogluconic trisodium Salt as a Drug Delivery System. Biomacromolecules. 2018;19(4):1294–304.
17. Yan Q, Chen X, Gong H, Qiu P, Xiao X, Dang S, Hong A, Ma Y. Delivery of a TNF-α-derived peptide by nanoparticles enhances its antitumor activity by inducing cell-cycle arrest and caspase-dependent apoptosis. FASEB J. 2018:fj201800377R. https://doi.org/10.1096/fj.201800377R.
18. Xing L, Fan YT, Zhou TJ, Gong JH, Cui LH, Cho KH, Choi YJ, Jiang HL, Cho CS. Chemical modification of chitosan for efficient vaccine delivery. Molecules. 2018;23(2):229.
19. De Masi A, Tonazzini I, Masciullo C, Mezzena R, Chiellini F, Puppi D, Cecchini M. Chitosan films for regenerative medicine: fabrication methods and mechanical characterization of nanostructured chitosan films. Biophys Revs. 2019;11(5):807–15.
20. Sultankulov B, Berillo D, Sultankulova K, Tokay T, Saparov A. Progress in the development of chitosan-based biomaterials for tissue engineering and regenerative medicine. Biomolecules. 2019;9(9):470.
21. Feng P, Luo Y, Ke C, Qiu H, Wang W, Zhu Y, Hou R, Xu L, Wu S. Chitosan-based functional materials for skin wound repair: mechanisms and applications. Front Bioeng Biotechnol. 2021;9(111). https://doi.org/10.3389/fbioe.2021.650598.
22. Chalongsuk R, Sribundit N. Usage of chitosan in Thai pharmaceutical and cosmetic industries. Sci Eng Health Stud. 2013;7:49–53.
23. Herdiana Y, Wathoni N, Shamsuddin S, Joni IM, Muchtaridi M. Chitosan-based nanoparticles of targeted drug delivery system in breast cancer treatment. Polymers. 2021;13(11):1717.
24. da Silva Júnior WF, de Oliveira Pinheiro JG, Moreira CD, de Souza FJ, de Lima AA. Chapter 15 - Alternative technologies to improve solubility and stability of poorly water-soluble drugs, in multifunctional systems for combined delivery, biosensing and diagnostics. In: Grumezescu AM, Editor. Elsevier; 2017. p. 281–305. https://doi.org/10.1016/B978-0-323-52725-5.00015-0.
25. Patra CN, Priya R, Swain S, Kumar JG, Panigrahi KC, Ghose D. Pharmaceutical significance of Eudragit: A review. Future J Pharm Sci. 2017;3(1):33–45.
26. Mehta R, Chawla A, Sharma P, Pawar P. Formulation and in vitro evaluation of Eudragit S-100 coated naproxen matrix tablets for colon-targeted drug delivery system. J Adv Pharm Technol Res. 2013;4(1):31–41.
27. Ou K, Liu Y, Deng L, Chen S, Gu S, Wang B. Covalently grafting polycation to bacterial cellulose for antibacterial and anti-cell adhesive wound dressings. Int J Biol Macromol. 2024;269:132157.
28. Din FU, Aman W, Ullah I, Qureshi OS, Mustapha O, Shafique S, Zeb A. Effective use of nanocarriers as drug delivery systems for the treatment of selected tumors. Int J Nanomedicine. 2017;12:7291–309.
29. Alsehli M. Polymeric nanocarriers as stimuli-responsive systems for targeted tumor (cancer) therapy: Recent advances in drug delivery. Saudi Pharm . 2020;28(3):255–65.
30. Saravanakumar G, Kim WJ. Stimuli-Responsive Polymeric Nanocarriers as Promising Drug and Gene Delivery Systems. In: Prokop A, Iwasaki Y, Harada A, editors. Intracellular Delivery II. Fundamental Biomedical Technologies, vol 7. 2014. Dordrecht: Springer; https://doi.org/10.1007/978-94-017-8896-0_4.
31. Seraji AA, Goharpey F, Yeganeh JK. Highly crystallized and tough polylactic acid through addition of surface modified cellulose nanocrystals. J Appl Polym Sci. 2022;139:e52871.
32. Mirabdali S, Ghafouri K, Farahmand Y, Gholizadeh N, Yazdani O, Esbati R, Hajiagha BS, Rahimi A. The role and function of autophagy through signaling and pathogenetic pathways and lncRNAs in ovarian cancer. Pathol Res Pract. 2024;253:154899.
33. Majumder J, Minko T. Multifunctional and stimuli-responsive nanocarriers for targeted therapeutic delivery. Exp Opin Drug Deliv. 2021;18(2):205–27.
34. Luo Y, Zhao J, Zhang X, Wang C, Wang T, Jiang M, Zhu Q, Xie T, Chen D. Size controlled fabrication of enzyme encapsulated amorphous calcium phosphate nanoparticle and its intracellular biosensing application. Colloids Surf B Biointerfaces. 2021;201:111638.
35. Maximova T, Moffatt R, Ma B, Nussinov R, Shehu A. Principles and overview of sampling methods for modeling macromolecular structure and dynamics. PLOS Comput Biol. 2016;12(4):e1004619.
36. Ferreira LG, Dos Santos RN, Oliva G, Andricopulo AD. Molecular Docking and Structure-Based Drug Design Strategies. Molecules. 2015;20(7):13384–421. https://doi.org/10.3390/molecules200713384.
37. Hospital A, Goñi JR, Orozco M, Gelpí JL. Molecular dynamics simulations: advances and applications. Adv Appl Bioinform Chem. 2015;8:37–47.
38. Tuszynski JA, Winter P, White D, Tseng C-Y, Sahu KK, Gentile F, Spasevska I, Omar SI, Nayebi N, Churchill CD, Klobukowski M, El-Magd RMA. Mathematical and computational modeling in biology at multiple scales. Theor Biol Med Model. 2014;11:52–52.
39. He X, Jiang Z, Akakuru OU, Li J, Wu A. Nanoscale covalent organic frameworks: from controlled synthesis to cancer therapy. Chem Commun. 2021;57(93):12417–35.
40. Malekshahi Y, Gheibi S, Ghiasvand N, Jafari F, Mirabdali S, Kiani A, Shokoohinia Y. Effects of prantschimgin and grandivitin from Ferulago macrocarpa on VEGF, MMP9, MMP2 and research of binding modes using computational methods. Pharm Int Acta. 2018;1:92–3. https://doi.org/10.22037/ipa.v1i1.20041.
41. Kabedev A, Hossain S, Hubert M, Larsson P, Bergström CAS. Molecular dynamics simulations reveal membrane interactions for poorly water-soluble drugs: impact of bile solubilization and drug aggregation. J Pharm Sci. 2021;110(1):176–85.
42. Loschwitz J, Olubiyi OO, Hub JS, Strodel B, Poojari CS. Computer simulations of protein-membrane systems. Prog Mol Biol Transl Sci. 2020;170:273–403.
43. Chng CP, Yang LW. Coarse-grained models reveal functional dynamics–II. Molecular dynamics simulation at the coarse-grained level–theories and biological applications. Bioinform Biol Insights. 2008;2:171–85.

44. Hasani-Sadrabadi MM, Taranejoo S, Dashtimoghadam E, Bahlakeh G, Majedi FS, VanDersarl JJ, Janmaleki M, Sharifi F, Bertsch A, Hourigan K, Tayebi L, Renaud P, Jacob KI. Microfluidic manipulation of core/shell nanoparticles for oral delivery of chemotherapeutics: a new treatment approach for colorectal cancer. Adv Mater. 2016;28(21):4134–41.
45. Kataoka Y, Yamada Y. Van der Waals type equation of state for Lennard-Jones fluid and the fluctuation of the potential energy by molecular dynamics simulations. Mol Simul. 2011;38:1–6.
46. Gilson MK, Honig B. Calculation of the total electrostatic energy of a macromolecular system: Solvation energies, binding energies, and conformational analysis. Proteins. 1988;4(1):7–18.
47. Kauffman GB. Inorganic Chemistry, 2nd Edition (Miessler, Gary L.; Tarr, Donald A.). J Chem Educ. 2000;77:165. https://doi.org/10.1021/ed077p165.1.

Publisher's Note